

Analyzing Core–Shell Structured Zinc Doped MgO Wrapped $\text{Ba}_{1-x}\text{Sr}_x\text{TiO}_3$ NanoparticlesJian Quan Qi,^{*,†,‡} Hu Yong Tian,[†] Yu Wang,[†] Geoffrey Kin Hung Pang,[†] Long Tu Li,[‡] and Helen Lai Wah Chan[†]*Department of Applied Physics and Materials Research Center, The Hong Kong Polytechnic University, Hong Kong, China, and Department of Materials Sciences & Engineering and State Key Laboratory of Fine Ceramics and New Processing, Tsinghua University, Beijing 100084, China**Received: April 5, 2005; In Final Form: May 15, 2005*

BST nanoparticles were directly synthesized from solution at 70 °C and then wrapped with zinc doped MgO in solution. This core–shell structure was analyzed by a conjunction of XRD, HRTEM, and FE-SEM. The lattice cell parameter of BST core was found to have shrinkage. The lattice cell mismatch between core and shell creates a variation of lattice cell parameter of BST core and we proposed a new method to estimate it by the XRD peak broadening effect. Two possible modes of matching the BST core and MZO shell were suggested and mode II was assigned to our core–shell structure by the observation of HRTEM and analysis of XRD data. Un-grown BST nanoparticles can also be observed by FE-SEM in fracture grains of the ceramics, which was sintered at 1350 °C.

1. Introduction

Core–shell structured nanoparticles have received much attention for their unique physical and chemical properties, as well as their technological applications.^{1–7} Core–shell structured nanoparticles with oxide shells are also interesting from a number of perspectives.^{8–11} The shells offer protection to the cores as well as introduce new properties to the hybrid structures.¹² $\text{Ba}_{0.5}\text{Sr}_{0.5}\text{TiO}_3$ (BST) materials, paraelectric at room temperature, are attractive candidates for several microwave electronic device applications, such as phase shifters, filters, varactors, delay lines, etc.^{13–15} However, significant reductions in loss at high frequencies together with improved dielectric tunability are needed for their realization in devices. One possible way is to use BST composites to obtain low-loss and low-K dielectric properties, e.g., MgO tailored BST composites to specific applications have been studied.^{13,16–18} The advantages of core–shell structures are that their properties can be conveniently tuned and tailored by designing the chemical compositions as well as sizes of the core and the shell. A strategy is the synthesis of MgO wrapped BST core–shell structured nanoparticles, using nanotechnology, and obtaining their ceramics or films to improve the properties. We synthesized MgO wrapped BST core–shell structured nanoparticles for microwave devices.¹⁹ To improve the sintering characteristics of these kinds of materials, ZnO dopants were added into the shell. Because the physical and chemical properties and performances of the core–shell nanoparticles strongly depend on their microstructure, which includes the structure of the core, the shell, and the interface,^{1–3,6} analysis of microstructures and their behavior is very important to both theory and applications. The analysis of the core–shell structure with a coherent interface is relatively simple for high-resolution transmission electron microscopy (HRTEM), but analysis of an incoherent or lattice-unmatched interface for core–shell particles is challenging, due to the small

size of the grains as well as the complex orientation.^{1,2} The mismatch of oxide core–shell structures often leads to a variation of lattice cell parameters, but it was rarely estimated in previous documents. In this study, the microstructures and annealing behavior of Zn-doped MgO (MZO) wrapped BST nanoparticles were analyzed by X-ray diffraction (XRD), field emission scanning electron microscopy (FE-SEM), and high-resolution transmission electron microscopy (HRTEM). The lattice mismatch was estimated by XRD and observed by HRTEM near the interface of the BST core and MgO shell. A new method was proposed to estimate the variation of lattice cell parameter with the XRD peak broadening effect.

2. Experimental Procedure

2.1. Synthesis of BST Nanoparticles from Solution. The BST nanoparticles were fabricated by the direct synthesis from solution (DSS) method as we previously reported.^{20,21} The typical synthesis procedure used high purity $\text{Ba}(\text{OH})_2 \cdot 8\text{H}_2\text{O}$, $\text{Sr}(\text{OH})_2 \cdot 8\text{H}_2\text{O}$, and $\text{Ti}(\text{OBU})_4$ as starting materials. The base solution was prepared by dissolving $\text{Ba}(\text{OH})_2 \cdot 8\text{H}_2\text{O}$ (31.55 g) and $\text{Sr}(\text{OH})_2 \cdot 8\text{H}_2\text{O}$ (26.56 g) into distilled water (500 mL). The concentration of the base solution was ~ 0.2 M. The solution was then heated to 70 °C in a water bath. The titanium solution was prepared by dissolving $\text{Ti}(\text{OBU})_4$ (68.07 g) into absolute ethanol (500 mL). These solution concentrations are for the composition of $(\text{Ba}_{0.5}\text{Sr}_{0.5})\text{TiO}_3$. The reaction took place by dripping the titanium solution into the base solution (70 °C) under vigorous stirring. An instantaneous formation of white precipitate was observed. After the reaction was completed, the white precipitate was obtained by filtration and baked at 70 °C for 24 h in an oven.

2.2. Wrapping the MZO Shell on BST Nanoparticles and Preparing the Ceramics. The BST nanoparticles were dispersed in distilled water by ball-grinding for 2 h. The solutions of magnesium nitrate hexahydrate ($\text{Mg}(\text{NO}_3)_2 \cdot 6\text{H}_2\text{O}$) and zinc nitrate hexahydrate ($\text{Zn}(\text{NO}_3)_2 \cdot 6\text{H}_2\text{O}$) were added to the BST suspension under vigorous stirring, and then ultrasonic agitation for 1 h. Ammonia was subsequently added to adjust the acidity

* Address correspondence to this author. E-mail: jianquanqi@mail.tsinghua.edu.cn. Phone: +852-2766-4616. Fax: +852-2333-7629.

[†] The Hong Kong Polytechnic University.

[‡] Tsinghua University.

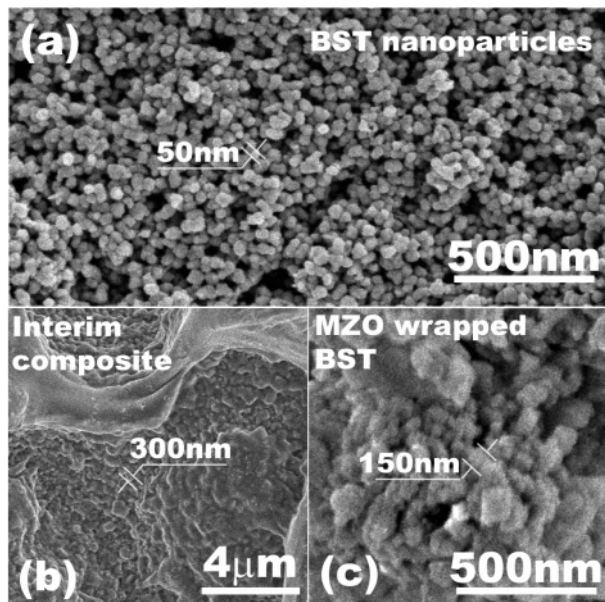


Figure 1. FE-SEM image: (a) $\text{Ba}_{1-x}\text{Sr}_x\text{TiO}_3$ nanoparticles prepared at 70 °C, (b) interim composite of MZO precursor wrapped BST nanoparticles, and (c) MZO wrapped BST nanoparticles annealed at 500 °C.

of the mixture to near pH ~ 11 . The resulting MZO-wrapped BST mixture was filtered out, carefully washed several times by deionized water, and then dried at 80 °C.

The powders with the core of BST nanoparticles and the shell of MZO precursors were annealing at different temperatures from 500 to 1000 °C to obtain the crystallized MZO shell. The MZO wrapped BST nanoparticle was pressed into disks with 1 mm thickness and 10 mm diameter and sintered at 1350 °C to obtain the ceramics.

2.3. Analysis of the Core–Shell Structures. Both BST nanoparticles, MZO wrapped BST core–shell structured nanoparticles annealing at different temperatures, and their ceramics were analyzed by means of X-ray diffraction (XRD) on a Philips Diffractometer (Model: X'Pert-Pro MPD), using Cu K α radiation (40 kV, 30 mA), scanning electron microscopy (SEM) on a JEOL field-emission SEM (Model: JSM 6335F NT), and transmission electron microscopy (TEM) on a JEOL TEM (Model: JSM2010) with a best point resolution of 0.24 nm at 200 kV, respectively.

3. Results and Discussions

The morphology of as-prepared BST nanoparticles and MZO wrapped BST powders can be observed by FE-SEM (Figure 1). The grains of as-prepared BST nanoparticles by the DSS method are rather homogeneous with a size of about 50 nm as shown in Figure 1a. Because the suspensions of BST nanoparticles by DSS in distilled water are alkaline with pH ~ 10 , the positively charged ions can be attracted and deposited on the surface of BST nanoparticles when the solutions of magnesium nitrate hexahydrate ($\text{Mg}(\text{NO}_3)_2 \cdot 6\text{H}_2\text{O}$) and zinc nitrate hexahydrate ($\text{Zn}(\text{NO}_3)_2 \cdot 6\text{H}_2\text{O}$) are added. The precursor of MZO and ammonia nitrate wrapped the BST nanoparticles and formed agglomerate with a size greater than 300 nm as shown in Figure 1b. The crystallization of the precursor of MZO happened at the annealing temperature of above 500 °C, and the size of the agglomerate was reduced as shown in Figure 1c.

The phases of the sample can be checked by XRD analysis as shown in Figure 2. To check the MgO phase clearly, The XRD profile of halite structured MZO ceramics also was given

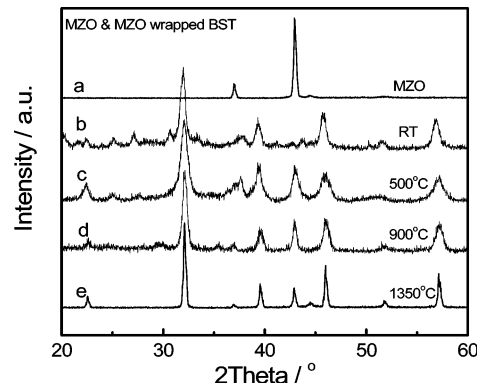


Figure 2. XRD profile of MZO wrapped BST nanoparticles annealing at different temperatures: (a) MZO ceramics, (b) as-prepared MZO precursor wrapped BST nanoparticles, (c) MZO wrapped BST nanoparticles annealed at 500 °C, (d) MZO wrapped BST nanoparticles annealed at 900 °C, and (e) ceramics of MZO wrapped BST nanoparticles sintered at 1350 °C.

in Figure 2a. There are no halite phase peaks and many other peaks exist which are indexed as ammonia nitrate except for BST peaks in the as-prepared powders as shown in Figure 2b because the MZO precursor is amorphous. After annealing or sintering at high temperature, the MZO precursor crystallized as the halite structure as shown in Figure 2, panels b, c, d, and e, respectively.

The lattice cell parameters can be estimated from the peak positions and for a cubic crystal,

$$a = d\sqrt{h^2 + k^2 + l^2} \quad (1)$$

where a is lattice parameter and d is the distance between a certain diffraction crystalline plane and the (hkl) crystalline plane index. d can be calculated from the Bragg's equation

$$\lambda = 2d \sin \theta \quad (2)$$

where λ is X-ray wavelength and θ is the diffraction angle.

The crystallite size of the powders can be estimated from the broadening of corresponding X-ray spectral peaks by the Scherrer's formula:

$$L = \frac{K\lambda}{\beta \cos \theta} \quad (3)$$

where L is the crystallite size and λ is the wavelength of the X-ray radiation (Cu K α = 0.15418 nm). K is usually taken as 0.89. β is the line width at half-maximum height after subtraction of equipment broadening and θ is the diffraction angle. In the calculation the XRD peak of the (200) plane of halite structured MZO ($2\theta \sim 43$) and the (200) plane of perovskite structured BST ($2\theta \sim 46$) were used.

The XRD profiles of the (200) plane of two phases in different samples annealed at different temperatures which are regressed by Gaussian fitting are shown in Figure 3, and the annealing temperature dependence of the lattice cell parameters and crystallite size estimated by XRD data from Figure 3 are shown in Figures 4 and 5.

The lattice cell parameter of MZO, a_{MZO} , increases with annealing temperature. There are many hydroxide groups compensated by cation vacancy in the MZO lattice cell and Zn ion, which is bigger (0.74 Å) than the Mg ion (0.72 Å), cannot solubilize into the MgO lattice completely, thus, the lattice cell parameter is small at 500 °C. When the annealing temperature increases, the cation vacancies removed with hydroxide groups

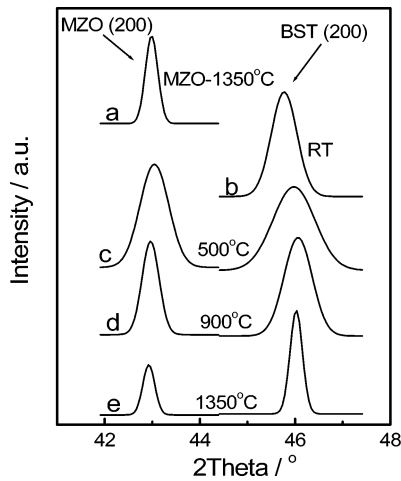


Figure 3. XRD profiles of the (200) crystalline plane of (a) MZO ceramics, (b) perovskite peak in MZO precursor wrapped BST nanoparticles, (c) MZO wrapped BST nanoparticles annealing at 500 °C, (d) MZO wrapped BST nanoparticles annealing at 900 °C, and (e) ceramics of MZO wrapped BST nanoparticles sintered at 1350 °C.

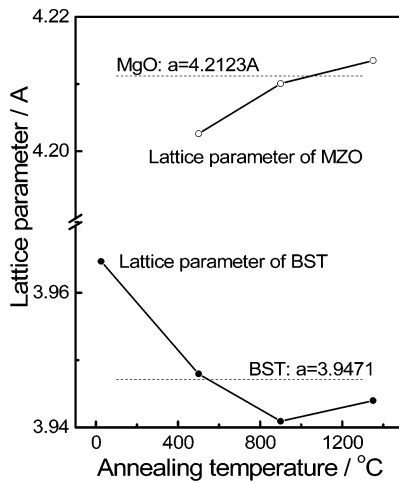


Figure 4. Lattice parameters of BST core and MZO shell as a function of annealing temperature.

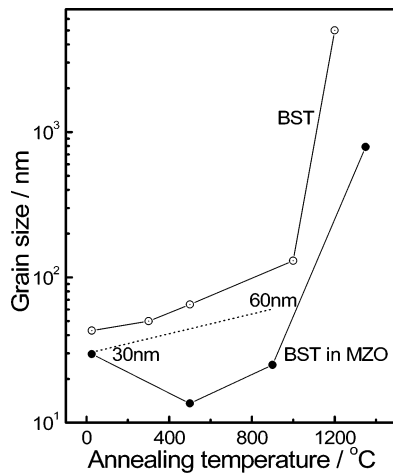


Figure 5. Annealing temperature dependence of the nominal crystallite size of BST as core in the MZO shell (solid circles) and that of pure BST nanoparticles (open circles).

release from the lattice and more Zn ions are introduced into the lattice, so that the lattice cell of MZO expands. It is noted that the BST lattice cell is smaller than that in JCPDS cards (no. 39-1395) at high temperature because the lattice cell of

the BST core is subjected to inner stress caused by the MZO shell crystallization from amorphous to halite structure.

It is easily understood that the crystallite size of pure BST increases with the annealing temperature for the grain growth even at not very high temperature because nanoparticles have much greater chemical activity than conventional powders in Figure 5. However, it should be noted that the nominal crystallite size of BST as core in MZO estimated from XRD data decreases before 500 °C and then increases with annealing temperature and the size for the sample annealed at 900 °C is smaller than the initial value. After the BST nanoparticles were wrapped in MZO and the MZO crystallized from amorphous to halite structure, the lattice mismatch can cause inner stress and lead to a variation of lattice cell parameter, which can cause XRD peaks to broaden. Therefore, we should consider this factor when we estimate the crystallite size by XRD peak broadening effects. Different mathematical methods exist (e.g., Langford,²² Balzar and Ledbetter,²³ and Warren–Averbach²⁴), which take into account strain in the analysis of XRD data, and these methods use the integral breadth or the entire peak profile. However, here we focus much attention on the lattice parameter variation and the half width by Gaussian peak fits are used to estimate it to simplify the model. Given a variation of the lattice cell parameter δa , the value of d changes by δd accordingly; according to Bragg's equation (eq 2), θ can change by $\delta\theta$ as eq 4.

$$\delta d = -\frac{\lambda \cos \theta}{2 \sin^2 \theta} \delta \theta \quad (4)$$

Here, the minus symbol indicates that when the lattice cell was subjected to inner stress and shrank, the peak position shifted to a high degree. Because a cubic lattice cell parameter can be calculated as eq 5:

$$\frac{1}{d^2} = \frac{h^2 + k^2 + l^2}{a^2} \quad (5)$$

the variation of the lattice cell parameter can be given as eq 6

$$\delta a = \delta d \sqrt{h^2 + k^2 + l^2} \quad (6)$$

Using Equation 4, the broadening of the XRD peak caused by lattice cell variation can be estimated as eq 7:

$$\delta \theta = -\frac{2 \sin \theta \tan \theta}{\lambda \sqrt{h^2 + k^2 + l^2}} \delta a \quad (7)$$

or the variation of lattice cell parameter can be given as eq 8

$$\delta a = -\frac{\lambda \sqrt{h^2 + k^2 + l^2}}{2 \sin \theta \tan \theta} \delta \theta \quad (8)$$

where $\delta\theta$ is the line width at half-maximum height of the XRD peak after subtraction of equipment broadening and nanoeffect broadening β (reference Scherrer formula, eq 3). Because in our core-shell structure, the MZO shell wraps the BST core and offers inert barriers around BST nanoparticles, it prohibits the grain growth of BST nanoparticles before sintering started at low annealing temperatures, e.g., <1000 °C. This conclusion can be confirmed by our observation of HRTEM. Therefore, the change of XRD peak broadening of BST caused by grain growth at low annealing temperature can be ignored. The variation of the lattice cell parameters is responsible for the increase in broadening of the XRD peak compared with the

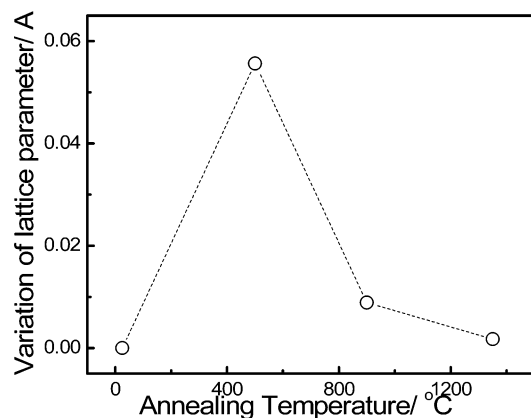


Figure 6. Variation of lattice cell parameters of the BST core as a function of annealing temperature.

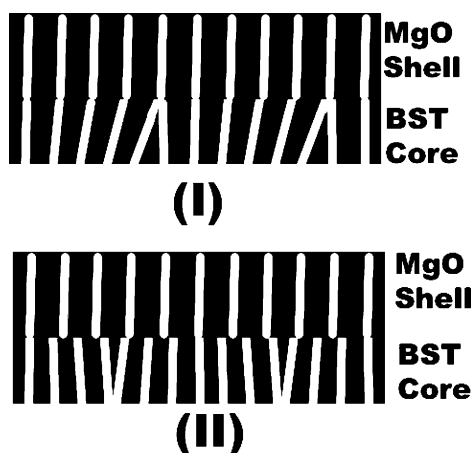


Figure 7. The lattice match modes between the BST core and the MZO shell.

initial as-prepared BST nanoparticles so that we can estimate it according to eq 8 as shown in Figure 6.

The maximum lattice cell variation is estimated to be 0.056 Å, almost 1.5% of 3.95 Å. This means that the BST lattice parameter of some lattice cells in the nanosized BST core can decrease to 3.902 Å from 3.958 Å (calculated by the XRD peak position, reference Figure 4). Therefore, the lattice mismatch in MZO wrapped BST nanoparticles is great and caused inner stress leading to shrinkage and variation in the lattice cell of the BST core, which can be estimated by the XRD peak position and the broadening effect.

There are two possible modes of lattice matching between the MgO and BST lattice as shown in Figure 7. The bright bars in the figure represent a certain match plane. The first mode, (I), is where the BST lattice matches the MgO lattice one to one and inserts dislocations when the mismatch is great enough. The BST cell will expand in this mode. The second mode, (II), is where the BST lattice mismatches the MgO lattice and inserts dislocation to match MgO. The BST cell should shrink in this mode. From XRD analytical results, the core-shell structure probably follows the second mode because the lattice cell parameter of BST nanoparticles decreases after being wrapped by MZO.

The interface of the BST core and the MZO shell is particularly important because its sharpness, lattice mismatch, and chemical gradient are critical for electron transfer and coupling. An epitaxial orientation relationship between the core and the shell is favorable, but an epitaxial growth is determined by their crystal structures.¹ The HRTEM image of the MZO

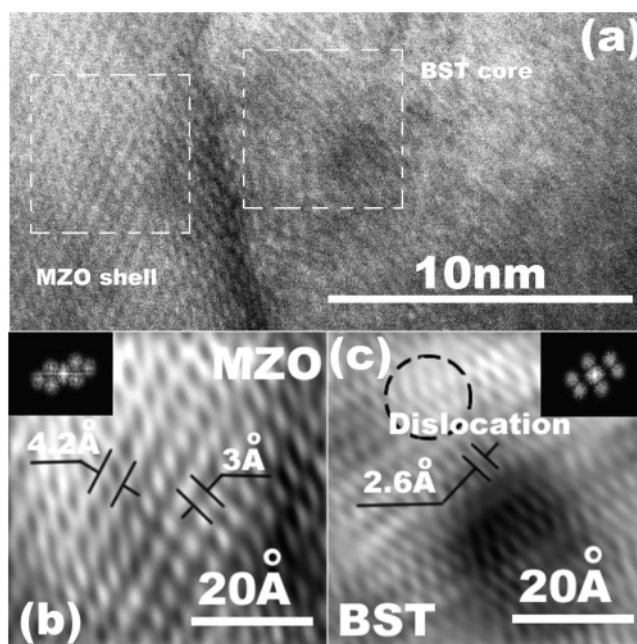


Figure 8. HRTEM image of the MZO wrapped BST core-shell structure: (a) interface of the core-shell structure, (b) lattice of the MZO shell, and (c) lattice of the BST core.

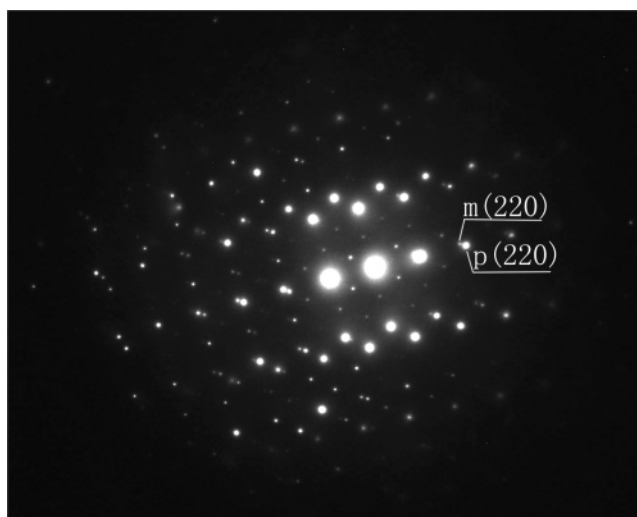


Figure 9. SEAD of the MZO wrapped BST core-shell structure (m(220) and p(220) represent the (220) plane of BST and MZO, respectively).

wrapped BST core-shell structure is shown in Figure 8. The interface of the core-shell structure is clearly shown in Figure 8a. The lattice structures of the MZO shell and the BST core framed in Figure 8a are shown in Figure 8, panels b and c, respectively. Panels b and c in Figure 8 are obtained by Fast Fourier Transform (FFT) and smoothing the edge using a mask (as the insets of Figure 8, panels b and c, respectively) and then inverse FFT. It can be observed clearly that the MZO shell and the BST core matched along their (110) planes. The BST lattice cell is smaller to the normal one especially near the match boundary. There are many dislocations in the BST lattice cell, and the integrity of the MZO lattice is better than that of the BST core. The distance between the (110) planes is estimated as 2.6 Å and the lattice cell parameter of BST is only 3.7 Å. Therefore, the lattice cell was depressed by the MZO shell as confirmed by XRD analysis.

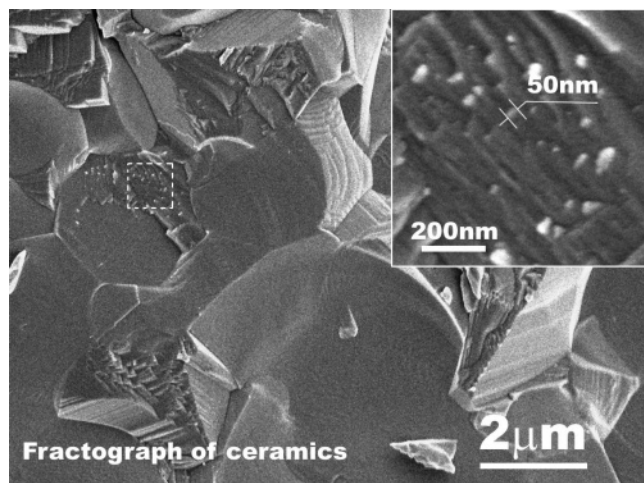


Figure 10. Fractograph of the MZO wrapped BST core-shell structured ceramics sintered at 1350 °C.

The MZO wrapped BST core-shell structure can also be checked by selected area electron diffraction (SAED) as shown in Figure 9. It can be observed that there is a spot of the diffraction plane of MZO beside that of the same diffraction plane of BST, labeled as $m(220)$ and $p(220)$ planes in the figure, showing that the lattice cells are matched between the core and the shell.

MZO wrapped core-shell structures also can be observed in a fractograph image by FE-SEM as shown in Figure 10. Both fractured styles, along grain boundaries and through grains, can be observed in the image. Some un-grown BST nanoparticles which keep their size as as-prepared ones also can be observed in fractured grains, but on the boundary, they can hardly be observed. This also confirmed that the effect of the inert MZO shell can protect the core of BST nanoparticles and be a barrier to the grain growth.

4. Conclusions

It is important to analyze the microstructures quantitatively for nanostructures, and the simultaneous application of XRD, HRTEM, SAED, and FE-SEM can offer an efficient way to determine the structure of MZO wrapped BST core-shell nanoparticles. From XRD analysis, the lattice cell parameters and crystallite size and variation of lattice parameter can be estimated. The XRD peak broadening effect can be associated with both the crystallite size effect and the variation of lattice cell parameters. The lattice mismatch between core and shell causes the variation and shrinkage of the lattice cell parameter

of the BST core. The details of the lattice match of the MZO shell and the BST core can be observed and analyzed by HRTEM and SAED, and a possible mode of lattice matching between the BST core and the MZO shell prepared by our method can be speculated. The morphology of MZO wrapped BST can be observed by FE-SEM. Un-grown BST nanoparticles also can be observed in fracture grains of the ceramics. The procedures and methodology presented here can be extended to the analysis of general nanoparticles that have a complex phase structure.

Acknowledgment. The author would like to acknowledge the financial support of the Postdoctoral Research Fellowship Scheme and the Center for Smart Materials of the Hong Kong Polytechnic University.

References and Notes

- (1) Li, J.; Zeng, H.; Sun, S. H.; Liu, J. P.; Wang, Z. L. *J. Phys. Chem. B* **2004**, *108*, 14005.
- (2) Danek, M.; Jensen, K. F.; Murray, C. B.; Bawendi, M. G. *Chem. Mater.* **1996**, *8*, 173.
- (3) Peng, X.; Schlamp, M. C.; Kadavanich, A. V.; Alivisatos, A. P. *J. Am. Chem. Soc.* **1997**, *119*, 7019.
- (4) Malik, M. A.; O'Brien, P.; Revaprasadu, N. *Chem. Mater.* **2002**, *14*, 2004.
- (5) Reiss, P.; Bleuse, J.; Pron, A. *Nano Lett.* **2002**, *2*, 781.
- (6) Skumryev, V.; Stoyanov, S.; Zhang, Y.; Hadjipanayis, G.; Givord, D.; Nogues, J. *Nature* **2003**, *423*, 850.
- (7) Zeng, H.; Li, J.; Wang, Z. L.; Liu, J. P.; Sun, S. H. *Nano Lett.* **2004**, *4*, 187.
- (8) Kakuta, N.; Park, K. H.; Finlayson, M. F.; Veno, A.; Bard, A. J.; Campion, A.; Fox, M. A.; Webber, S. E.; White, J. M. *J. Phys. Chem.* **1985**, *89*, 3828.
- (9) Nasr, C.; Hotchandani, S.; Kim, W. Y.; Schmehl, R. H.; Kamat, P. V. *J. Phys. Chem. B* **1997**, *101*, 7480.
- (10) Davis, S. S. *Trends. Biotechnol.* **1997**, *15*, 217.
- (11) Suryanarayanan, V.; Sreekumaran, N. A.; Tom, R. T.; Pradeep, T. *J. Mater. Chem.* **2004**, *14*, 2661.
- (12) Pastoriza-Santos, I.; Koktysh, D. S.; Mamedov, A. A.; Giersig, M.; Kotov, N. A.; Liz-Marzan, L. M. *Langmuir* **2000**, *16*, 2731.
- (13) Chang, W.; Sengupta, L. *J. Appl. Phys.* **2002**, *92*, 3941.
- (14) Gevorgian, S. S.; Kollberg, E. L. *IEEE Trans. Microwave Theory Tech.* **2001**, *49*, 2117.
- (15) Korn, D. S.; Wu, H. D. *Integr. Ferroelectr.* **1999**, *24*, 215.
- (16) Tseng, T. Y.; Lee, S. Y. *Appl. Phys. Lett.* **2003**, *83*, 981.
- (17) Jain, M.; Majumder, S. B.; Katiyar, R. S. *Appl. Phys. Lett.* **2002**, *81*, 3212.
- (18) Lee, S. Y.; Tseng, T. Y. *Appl. Phys. Lett.* **2002**, *80*, 1797.
- (19) Tian, H. Y.; Qi, J. Q.; Wang, Y.; Wang, J.; Chan, H. L. W.; Choy, C. L. *Nanotechnology* **2005**, *16*, 47.
- (20) Qi, J. Q.; Li, L. T.; Wang, Y. L.; Gui, Z. L. *J. Cryst. Growth* **2004**, *260*, 551.
- (21) Qi, J. Q.; Wang, Y.; Chen, W. P.; Li, L. T.; Chan, H. L. W. *J. Solid State Chem.* **2005**, *178*, 279.
- (22) Rand, M.; Langford, J. I.; Drake, A.; Abell, J. S. *Cryogenics* **1993**, *33*, 291.
- (23) Balzar, D.; Ledbetter, H. *Adv. X-ray Anal.* **1995**, *38*, 397.
- (24) Warren, B. E.; Averbach, B. L. *J. Appl. Phys.* **1950**, *21*, 595.